Supplementary Materials for

Discerning Rise Time Constants to Quantify Charge Carrier Extraction in Perovskite Solar Cells

Sandheep Ravishankar,[1*] Lennard Kruppa[1], Sandra Jenatsch[2], Genghua Yan[1], Yueming Wang[1]
[1]IEK-5 Photovoltaik, Forschungszentrum Jülich, 52425 Jülich, Germany
[2]Fluxim AG, Katharina-Sulzer-Platz 2, 8406 Winterthur, Switzerland

*author for correspondence, email: s.ravi.shankar@fz-juelich.de

This file includes:

Supplementary text
Figs. S1 to S10
Tables S1 to S2
References 48 to 52

A1. Discussion of simulation parameters

Relative permittivity: The relative permittivity value for the transport layers was chosen as 3, since typical values for fullerenes lie between 2 and 4.[48] The relative permittivity of the perovskite layer was set arbitrarily high to ensure no electric field inside the perovskite layer. However, the simulations in figure 4 in the main paper use the perovskite permittivity chosen from ref.[49].

Bandgap: The PTAA layer bandgap was chosen from ref.[50]. The perovskite bandgap was chosen arbitrarily. The PCBM layer bandgap was chosen based on ref.[51].

Electron affinities: The perovskite electron affinity was slightly modified from the value reported in ref.[50]. For simplicity, no band offsets were considered at the perovskite/transport layer interface. Therefore, the electron affinities were chosen based on the bandgaps in table S1.

Effective density of states (DOS): The effective DOS for the conduction and valence band of the perovskite layer was chosen from ref.[52]. The DOS of the transport layers were chosen to be the same as that of the perovskite layer for simplicity.

Radiative recombination coefficient: The order of the perovskite layer radiative recombination coefficient was chosen from ref. [52]. No recombination in the contact layers was assumed.

Mobilities: The electron and hole mobilities were set equal in all cases for simplicity. Based on the generally large mobilities reported for perovskite layers,[29] we chose a value of 20 cm^2/Vs. For the equivalent circuit simulations, the mobility is considered high enough to create a uniform carrier concentration in the perovskite layer and its value is hence unneeded.

Ion densities: Ionic effects in perovskite solar cells are known to occur at low frequencies (below 10^3 Hz).[40] Since we are interested in only electronic processes within the perovskite solar cell, we set the ion densities to zero and focus only on the high frequency region of the spectra. However, the simulations in figure 4 in the main paper include ionic densities.

Trap densities and capture coefficients: We focus on the effects of deep traps on the perovskite solar cell response and hence choose trap densities at mid-gap for the simulations. The trap density was chosen arbitrarily and the capture coefficients were set to obtain Shockley-Read-Hall lifetimes of 10^{-7} s for electrons and holes.

Built-in electrostatic voltage: The built-in electrostatic voltage in the transport layers was chosen arbitrarily, with a factor 2 assigned to the modification of this electrostatic voltage by the external voltage by assuming that the external voltage is split equally between the two transport layers to modify their respective electrostatic voltage.

A2. Derivation of the charge carrier exchange model

We consider the continuity equation for the perovskite bulk, shown in equation 5 in the main paper. Applying a small perturbation and removing steady-state terms, we obtain

$$\frac{d\tilde{n}}{dt} = \frac{\tilde{J}_\Phi}{qd} - \frac{\tilde{n}}{\tau_{rec}} - \frac{\tilde{J}_{exc}}{qd} \quad . \tag{S1}$$

To obtain the modulated carrier density, we apply a small perturbation to equation 4 in the main paper and using the Taylor expansion, we obtain

$$\tilde{n} = \left(\frac{dn}{dV_{int}}\right)\tilde{V}_{int} = \frac{qn}{2k_BT}\tilde{V}_{int} = \frac{C_\mu}{qd}\tilde{V}_{int} \quad , \tag{S2}$$

where C_μ is the chemical capacitance, given by

$$C_\mu = \frac{q^2 dn_i}{2k_BT}\exp\left(\frac{qV_{int}}{2k_BT}\right) \quad . \tag{S3}$$

The modulated exchange current density can be obtained by applying a small perturbation to equation 7 in the main paper and using the Taylor expansion, as

$$\tilde{J}_{exc} = \frac{C_\mu}{\tau_{exc}}\tilde{V}_{int} - \frac{1}{R_{exc}}\tilde{V}_{elec} \quad , \tag{S4}$$

where τ_{exc} is the charge carrier exchange lifetime that determines the speed at which charge carriers are injected (extracted) into (from) the bulk of the perovskite layer, given by

$$\tau_{exc} = \frac{d}{S_{exc}} \tag{S5}$$

and the exchange resistance R_{exc} across which the potential drop in the transport layer occurs, is given by

$$R_{exc} = \frac{2k_BT}{q^2 n_i S_{exc}}\exp\left(\frac{-qV_{elec}}{2k_BT}\right) \quad . \tag{S6}$$

Substituting equations S3 and S4 in equation S1, we obtain

$$C_\mu\frac{d\tilde{V}_{int}}{dt} = \tilde{J}_\Phi - C_\mu\left(\frac{1}{\tau_{exc}} + \frac{1}{\tau_{rec}}\right)\tilde{V}_{int} + \frac{\tilde{V}_{elec}}{R_{exc}} \quad , \tag{S7}$$

with R_{rec} being the recombination resistance, given by

$$R_{rec} = \frac{\tau_{rec}}{C_\mu} \quad . \tag{S8}$$

The balance of the current density in the device is obtained by including the capacitive discharge $\tilde{J}_{cap}$ from the electrodes to obtain the current density at the terminals as

$$\tilde{J} = \tilde{J}_{exc} - \tilde{J}_{cap} = \tilde{J}_{exc} - C_g\frac{d\tilde{V}_{elec}}{dt} \quad , \tag{S9}$$

where C_g is the geometric capacitance. Substituting equation S4 in equation S9, we obtain

$$C_g\frac{d\tilde{V}_{elec}}{dt} = \frac{C_\mu}{\tau_{exc}}\tilde{V}_{int} - \frac{\tilde{V}_{elec}}{R_{exc}} - \tilde{J} \quad . \tag{S10}$$

The relation between V_{elec} and the external voltage V_{ext} is given by

$$\tilde{V}_{elec} = \tilde{V}_{ext} + R_s\tilde{J} \quad , \tag{S11}$$

where R_s is the external series resistance. Substituting equation S11 in equations S7 and S10, we obtain

$$C_\mu\frac{d\tilde{V}_{int}}{dt} = \tilde{J}_\Phi - C_\mu\left(\frac{1}{\tau_{exc}} + \frac{1}{\tau_{rec}}\right)\tilde{V}_{int} + \frac{\tilde{V}_{ext}}{R_{exc}} + \frac{R_s}{R_{exc}}\tilde{J}, \tag{S12}$$

$$C_g\frac{d\tilde{V}_{ext}}{dt} = \frac{C_\mu}{\tau_{exc}}\tilde{V}_{int} - \frac{\tilde{V}_{ext}}{R_{exc}} - \left(1 + \frac{R_s}{R_{exc}} + R_s C_g\frac{d}{dt}\right)\tilde{J}. \tag{S13}$$

Equations S12-S13 represent a set of coupled, linear differential equations whose solution allows calculating the response of the solar cell to a small perturbation of current, voltage or light intensity. An alternate way of representing these equations is in the form of a matrix, given by

$$\begin{pmatrix} C_\mu & 0 \\ 0 & C_g \end{pmatrix}\begin{pmatrix} \frac{d\tilde{V}_{int}}{dt} \\ \frac{d\tilde{V}_{ext}}{dt} \end{pmatrix} = \begin{pmatrix} -\frac{C_\mu}{\tau_{exc}} - \frac{C_\mu}{\tau_{rec}} & \frac{1}{R_{exc}} \\ \frac{C_\mu}{\tau_{exc}} & -\frac{1}{R_{exc}} \end{pmatrix}\begin{pmatrix} \tilde{V}_{int} \\ \tilde{V}_{ext} \end{pmatrix} + \begin{pmatrix} 1 & \frac{R_s}{R_{exc}} \\ 0 & -1 - \frac{R_s}{R_{exc}} - R_s C_g\frac{d}{dt} \end{pmatrix}\begin{pmatrix} \tilde{J}_\Phi \\ \tilde{J} \end{pmatrix}. \tag{S14}$$

For the specific case of TPC and TPV measurements, we assume a delta pulse at $t=0$ for the modulated illumination $\tilde{J}_\Phi$ and set the corresponding unmodulated quantities ($\tilde{V}_{ext}$ in TPC and $\tilde{J}$ in TPV) to 0. In the case of TPV, the open-circuit condition implies that $V_{int} = V_{elec} = V_{ext}$, which allows defining the additional relation

$$\tau_{\text{exc}}(V_{\text{oc}}) = R_{\text{exc}}(V_{\text{oc}}) \times C_\mu(V_{\text{oc}}) = \frac{d}{S_{\text{exc}}(V_{\text{oc}})} \quad . \tag{S15}$$

We therefore obtain the matrices for TPC and TPV as

TPC

$$\begin{pmatrix} C_\mu & 0 \\ 0 & C_g R_s \end{pmatrix} \begin{pmatrix} d\widetilde{V}_{\text{int}}/dt \\ d\tilde{\jmath}/dt \end{pmatrix} = \begin{pmatrix} -\dfrac{C_\mu}{\tau_{\text{exc}}} - \dfrac{C_\mu}{\tau_{\text{rec}}} & \dfrac{R_s}{R_{\text{exc}}} \\ \dfrac{C_\mu}{\tau_{\text{exc}}} & -1 - \dfrac{R_s}{R_{\text{exc}}} \end{pmatrix} \begin{pmatrix} \widetilde{V}_{\text{int}} \\ \tilde{\jmath} \end{pmatrix}. \tag{S16}$$

TPV

$$\begin{pmatrix} C_\mu & 0 \\ 0 & C_g \end{pmatrix} \begin{pmatrix} d\widetilde{V}_{\text{int}}/dt \\ d\widetilde{V}_{\text{ext}}/dt \end{pmatrix} = \begin{pmatrix} -\dfrac{1}{R_{\text{exc}}} - \dfrac{1}{R_{\text{rec}}} & \dfrac{1}{R_{\text{exc}}} \\ \dfrac{C_\mu}{\tau_{\text{exc}}} & -\dfrac{1}{R_{\text{exc}}} \end{pmatrix} \begin{pmatrix} \widetilde{V}_{\text{int}} \\ \widetilde{V}_{\text{ext}} \end{pmatrix}. \tag{S17}$$

The matrices in equations S16-S17 are of the form $C\dot{X} = AX + B$, where X is the matrix that contains the variables that need to be solved for ($\widetilde{V}_{\text{int}}$ and either $\widetilde{V}_{\text{ext}}$ or $\tilde{\jmath}$) and the overdot indicates the first differential in time. The solution is thus given by

$$X = D\vec{v}_1 e^{-\lambda_1 t} + E\vec{v}_2 e^{-\lambda_2 t} \quad , \tag{S18}$$

where D and E are constants, $\vec{v}_1$ and $\vec{v}_2$ are the 2 x 1 eigenvectors of the $C^{-1}A$ matrix and λ_1 and λ_2 are the eigenvalues of the $C^{-1}A$ matrix. The time constants are obtained from the inverse eigenvalues i.e. $\tau_1 = 1/\lambda_1$ and $\tau_2 = 1/\lambda_2$. Using the initial condition of the photocurrent or photovoltage deflection being 0 at t=0, we obtain the photocurrent deflection in a TPC measurement as

$$\Delta j(t) = \Delta j_0 \left(e^{\frac{-t}{\tau_{\text{j,decay}}}} - e^{\frac{-t}{\tau_{\text{j,rise}}}} \right) \tag{S19}$$

and the external voltage deflection ΔV_{ext} in a TPV measurement as

$$\Delta V_{\text{ext}}(t) = \Delta V_{\text{ext,0}} \left(e^{\frac{-t}{\tau_{\text{V,decay}}}} - e^{\frac{-t}{\tau_{\text{V,rise}}}} \right). \tag{S20}$$

The analytical solutions from the model for the rise and decay time constants obtained from TPV measurements are

$$\tau_{\text{V,rise}} = \frac{2}{k_1 + k_2 + k_3 + \sqrt{(k_1 + k_2 + k_3)^2 - 4k_1 k_3}} \quad , \tag{S21}$$

$$\tau_{\text{V,decay}} = \frac{2}{k_1 + k_2 + k_3 - \sqrt{(k_1 + k_2 + k_3)^2 - 4k_1 k_3}} \quad , \tag{S22}$$

and the time constants in the case of TPC measurements are

$$\tau_{\text{j,rise}} = \frac{2}{k_1 + k_2 + k_3 + k_4 + \sqrt{(k_1 + k_2 + k_3 + k_4)^2 - 4(k_1 k_3 + k_1 k_4 + k_2 k_4)}} \quad , \tag{S23}$$

$$\tau_{\text{j,decay}} = \frac{2}{k_1 + k_2 + k_3 + k_4 - \sqrt{(k_1 + k_2 + k_3 + k_4)^2 - 4(k_1 k_3 + k_1 k_4 + k_2 k_4)}} \quad , \tag{S24}$$

where

$$k_1 = \frac{1}{\tau_{\text{rec}}} \quad ,$$

$$k_2 = \frac{1}{\tau_{\text{exc}}} \quad ,$$

$$k_3 = \frac{1}{R_{\text{exc}} C_g} \quad ,$$

$$k_4 = \frac{1}{R_s C_g} \quad . \tag{S25}$$

A3. Calculation of the time constant from -imag W

The IMVS transfer function given by equation 18 in the main paper is

$$W = W_0 \left(\frac{\tau_{\text{V,decay}}}{1 + i\omega\tau_{\text{V,decay}}} - \frac{\tau_{\text{V,rise}}}{1 + i\omega\tau_{\text{V,rise}}} \right), \tag{S26}$$

3

where W_0 is a constant. We consider a situation where the decay of the photovoltage is much slower than the rise of the photovoltage i.e. $\tau_{\text{V,decay}} \gg \tau_{\text{V,rise}}$. The negative imaginary part of W is then given by

$$-\text{imag } W = W_0 \left(\frac{\omega \tau_{\text{V,decay}}^2}{1 + \omega^2 \tau_{\text{V,decay}}^2} - \frac{\omega \tau_{\text{V,rise}}^2}{1 + \omega^2 \tau_{\text{V,rise}}^2} \right), \tag{S27}$$

where W_0 is a pre-factor. Differentiating equation S27 versus angular frequency ω, we obtain

$$\frac{d(-\text{imag } W)}{d\omega} = W_0 \left(\frac{\tau_{\text{V,decay}}^2 \left(1 - \omega^2 \tau_{\text{V,decay}}^2\right)}{\left(1 + \omega^2 \tau_{\text{V,decay}}^2\right)^2} - \frac{\tau_{\text{V,rise}}^2 \left(1 - \omega^2 \tau_{\text{V,rise}}^2\right)}{\left(1 + \omega^2 \tau_{\text{V,rise}}^2\right)^2} \right). \tag{S28}$$

The characteristic frequencies are calculated by setting the LHS of equation S28 to zero. We thus obtain

$$0 = \left(\tau_{\text{V,decay}}^2 - \omega_{\text{char}}^2 \tau_{\text{V,decay}}^4\right)\left(1 + 2\omega_{\text{char}}^2 \tau_{\text{V,rise}}^2 + \omega_{\text{char}}^4 \tau_{\text{V,rise}}^4\right) - \left(\tau_{\text{V,rise}}^2 - \omega_{\text{char}}^2 \tau_{\text{V,rise}}^4\right)\left(1 + 2\omega_{\text{char}}^2 \tau_{\text{V,decay}}^2 + \omega_{\text{char}}^4 \tau_{\text{V,decay}}^4\right). \tag{S29}$$

Dividing both sides of equation S29 by $\tau_{\text{V,decay}}^4$ and noting that $\left(\tau_{\text{V,rise}}/\tau_{\text{V,decay}}\right)^2 \to 0$, we obtain

$$\omega_{\text{char}} = \frac{1}{\tau_{\text{V,decay}}}. \tag{S30}$$

Therefore, when the time constants $\tau_{\text{V,decay}}$ and $\tau_{\text{V,rise}}$ are well separated in magnitude, the negative imaginary part of the transfer function plotted versus ω shows only the larger (slower) of the time constants as its maximum.

A4. Calculation of the time constants from -imag M_W

The negative imaginary part of the transformed IMVS transfer function is given from equation 21 in the main paper by

$$-\text{imag } M_{\text{W}} = M_{\text{W,0}} \left(\frac{\omega \tau_{\text{V,rise}}}{1 + \omega^2 \tau_{\text{V,rise}}^2} - \frac{\omega \tau_{\text{V,decay}}}{1 + \omega^2 \tau_{\text{V,decay}}^2} \right), \tag{S31}$$

where $M_{\text{W,0}}$ is a constant. Differentiating equation S31 versus angular frequency ω, we obtain

$$\frac{d(-\text{imag } M_{\text{W}})}{d\omega} = M_{\text{W,0}} \left(\frac{\tau_{\text{V,rise}}\left(\left(1 + \omega^2 \tau_{\text{V,rise}}^2\right) - 2\omega^2 \tau_{\text{V,rise}}^2\right)}{\left(1 + \omega^2 \tau_{\text{V,rise}}^2\right)^2} - \frac{\tau_{\text{V,decay}}\left(\left(1 + \omega^2 \tau_{\text{V,decay}}^2\right) - 2\omega^2 \tau_{\text{V,decay}}^2\right)}{\left(1 + \omega^2 \tau_{\text{V,decay}}^2\right)^2} \right). \tag{S32}$$

The characteristic frequencies are obtained by setting the LHS of equation S32 to zero, yielding

$$C^3 x^3 - C(3C + D)x^2 - (3C + D)x + 1 = 0, \tag{S33}$$

where $x = \omega_{\text{char}}^2$, $C = \tau_{\text{V,decay}}\tau_{\text{V,rise}}$ and $D = \tau_{\text{V,decay}}^2 + \tau_{\text{V,rise}}^2$. Solving numerically for the roots of equation S33 yields the rise and decay time constants from $\tau_{\text{char}} = 1/\omega_{\text{char}}$.

A5. Calculation of the amplitude of the negative real part of W

The IMVS transfer function from equation 18 in the main paper is given by

$$W = W_0 \left(\frac{\tau_{\text{V,decay}}}{1 + i\omega\tau_{\text{V,decay}}} - \frac{\tau_{\text{V,rise}}}{1 + i\omega\tau_{\text{V,rise}}} \right). \tag{S34}$$

The real part of equation S34 is given by

$$\text{real } W = W_0 \left(\frac{\tau_{\text{V,decay}}}{1 + \omega^2 \tau_{\text{V,decay}}^2} - \frac{\tau_{\text{V,rise}}}{1 + \omega^2 \tau_{\text{V,rise}}^2} \right). \tag{S35}$$

For well-separated time constants in magnitude ($\tau_{\text{V,rise}} \ll \tau_{\text{V,decay}}$), equation S35 can be approximated using the Taylor expansion at high frequencies as

$$\text{real } W = W_0 \left(\frac{1}{\omega^2 \tau_{\text{V,decay}}} - \frac{\tau_{\text{V,rise}}}{1 + \omega^2 \tau_{\text{V,rise}}^2} \right). \tag{S36}$$

Equation S36 transitions to negative values at high frequencies, with a corresponding minimum. We calculate the amplitude of this transition by finding the root ω_{min} of the derivative of real W versus ω and plugging it back in equation S36. We thus obtain

$$\text{real } W(\omega_{\min}) = W_0\left(-\frac{\tau_{V,\text{rise}}}{\frac{\tau_{V,\text{rise}}}{\tau_{V,\text{decay}}-\tau_{V,\text{rise}}}+\sqrt{\frac{\tau_{V,\text{decay}}\tau_{V,\text{rise}}}{\tau_{V,\text{decay}}-\tau_{V,\text{rise}}}}+1}+\right.$$

$$\left.\frac{\tau_{V,\text{rise}}^2}{\frac{\tau_{V,\text{decay}}\tau_{V,\text{rise}}}{\tau_{V,\text{decay}}-\tau_{V,\text{rise}}}+\sqrt{\frac{\tau_{V,\text{decay}}\tau_{V,\text{rise}}}{\tau_{V,\text{decay}}-\tau_{V,\text{rise}}}}}\right). \tag{S37}$$

For well-separated time constants, we have the approximations $\tau_{V,\text{decay}} - \tau_{V,\text{rise}} \cong \tau_{V,\text{decay}}$ and $\tau_{V,\text{rise}}/\tau_{V,\text{decay}} \cong 0$. Therefore, equation S37 simplifies to

$$\text{real } W(\omega_{\min}) = -W_0\tau_{V,\text{rise}} . \tag{S38}$$

A6. Subtraction of R_s from impedance transfer function to obtain M_Z

We consider a general impedance Z_1 given by

$$Z_1 = Z_1'(\omega) + iZ_1''(\omega) , \tag{S39}$$

where the real and imaginary parts are denoted using $'$ and $''$ respectively. We transform the impedance transfer function to M_{Z_1}, given by

$$M_{Z_1} = i\omega Z_1 = i\omega Z_1' - \omega Z_1'' . \tag{S40}$$

The characteristic frequency ω_1 is thus obtained from the peak of the negative imaginary part of M_{Z_1} given by

$$\frac{d(-\text{imag}(M_{Z_1}))}{d\omega} = 0 = -\left(Z_1' + \omega\frac{dZ_1'}{d\omega}\right) \rightarrow \omega_1 = \frac{-Z_1'(\omega_1)}{\left(\frac{dZ_1'}{d\omega}\Big|_{\omega=\omega_1}\right)} . \tag{S41}$$

We now consider an impedance Z_2 given by

$$Z_2 = R_s + Z_1 , \tag{S42}$$

where R_s is the series resistance. The corresponding transformed transfer function M_{Z_2} is

$$M_{Z_2} = i\omega Z_2 = i\omega(R_s + Z_1') - \omega Z_1'' . \tag{S43}$$

The characteristic frequency ω_2 is thus calculated from the peak of the negative imaginary part of the transfer function in equation S43 as

$$\omega_2 = \frac{-(R_s + Z_1'(\omega_2))}{\left(\frac{dZ_1'}{d\omega}\Big|_{\omega=\omega_2}\right)} . \tag{S44}$$

Equation S44 shows that the characteristic frequency ω_2 of the modified transfer function M_Z is influenced by the series resistance and is equal to the characteristic frequency ω_1 without a series resistance only when R_s tends to zero. We therefore subtract the series resistance from the measured spectra to remove the influence of R_s.

A7. Derivation of current-voltage curve equation with the influence of non-ideal charge extraction

We consider a PSC with an intrinsic perovskite layer of thickness d. The steady-state current density is given by

$$j = qd(G - R) = qd\left(G - \left(\frac{n-n_i}{\tau_{\text{rec}}}\right)\right) , \tag{S45}$$

where G is the generation rate, R is the recombination rate, n is the carrier concentration, n_i is the intrinsic carrier concentration and τ_{rec} is the recombination lifetime. To include the effect of non-ideal charge extraction, we replace the LHS of equation S45 with the expression for the exchange current density using equation 7 in the main paper, as

$$qn_iS_{exc}\left(\exp\left(\frac{qV_{int}}{2k_BT}\right) - \exp\left(\frac{qV_{elec}}{2k_BT}\right)\right) = qd\left(G - \left(\frac{n-n_i}{\tau_{rec}}\right)\right). \tag{S46}$$

Using the relations

$$n = n_i\exp\left(\frac{qV_{int}}{2k_BT}\right) \tag{S47}$$

and

$$\tau_{exc} = \frac{d}{S_{exc}} \tag{S48}$$

in equation S46, we obtain

$$n = \frac{G + \frac{n_i}{\tau_{rec}} + \frac{n_i}{\tau_{exc}}\exp\left(\frac{qV_{elec}}{2k_BT}\right)}{\left(\frac{1}{\tau_{exc}} + \frac{1}{\tau_{rec}}\right)}. \tag{S49}$$

Substituting equation S49 in equation S45, we obtain

$$j = \left(\frac{1}{1 + \frac{\tau_{exc}}{\tau_{rec}}}\right)qd\left(G - \frac{n_i}{\tau_{exc}}\left(\exp\left(\frac{qV_{elec}}{2k_BT}\right) - 1\right)\right). \tag{S50}$$
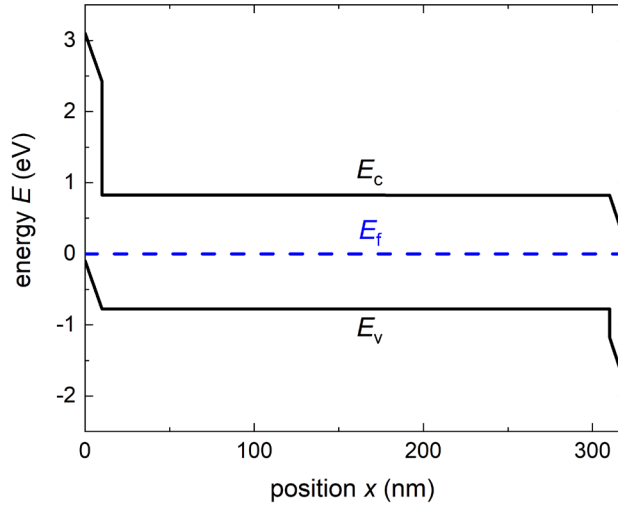

Figure S1 Band diagram of the perovskite solar cell used for the SETFOS simulations. No conduction band offset and valence band offset was considered at the perovskite/electron transport layer and perovskite/hole transport layer interfaces respectively. The permittivity of the perovskite was increased arbitrarily to ensure no electric field in the perovskite layer. No ionic densities were considered in this simulation. Band diagrams that include ionic densities in the perovskite layer are shown in figure 4 in the main paper.
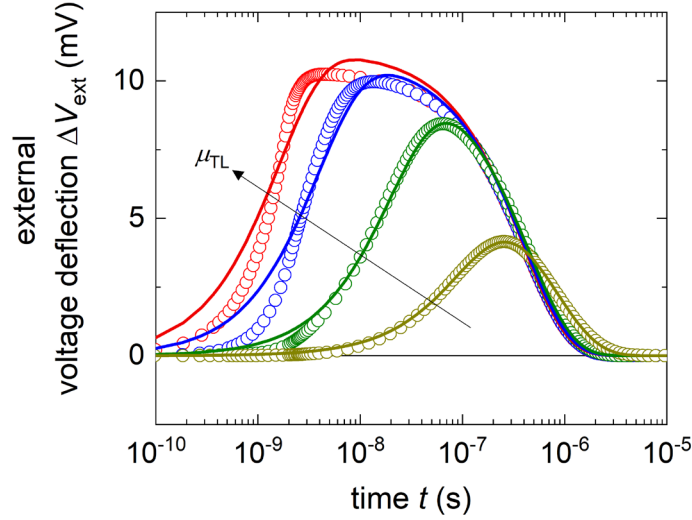
Figure S2 Fitting (solid lines) of the simulated TPV spectra (open symbols) in figure 2(a) in the main paper, using equation 11 in the main paper. The highest transport layer mobility corresponds to the situation $\mu_{TL} = \mu_{pero}$.
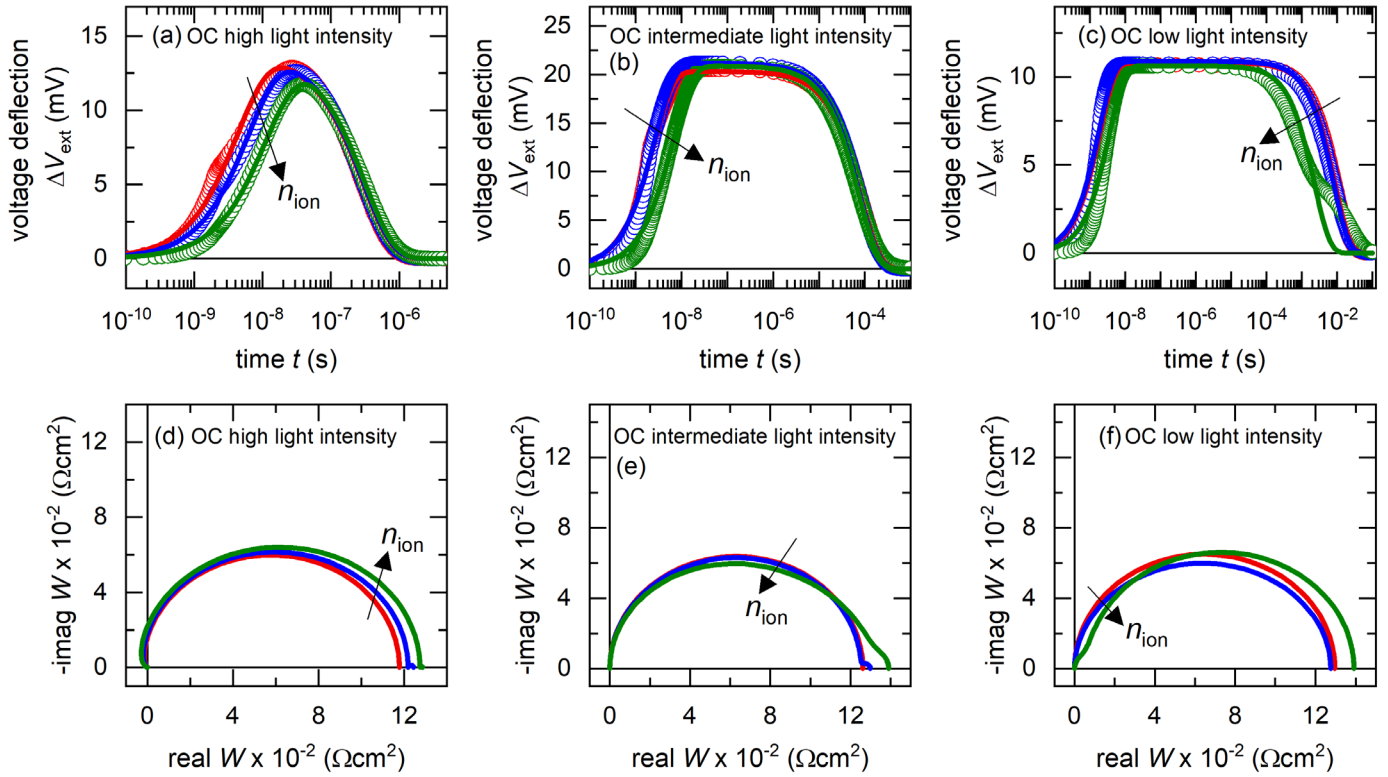

Figure S3 Drift-diffusion simulations of TPV (a, b and c) and IMVS (d, e and f) spectra at open-circuit conditions under different light intensities, for varying densities of mobile ions in the perovskite layer. The time constants obtained from these spectra are shown in figure 4 in the main paper.
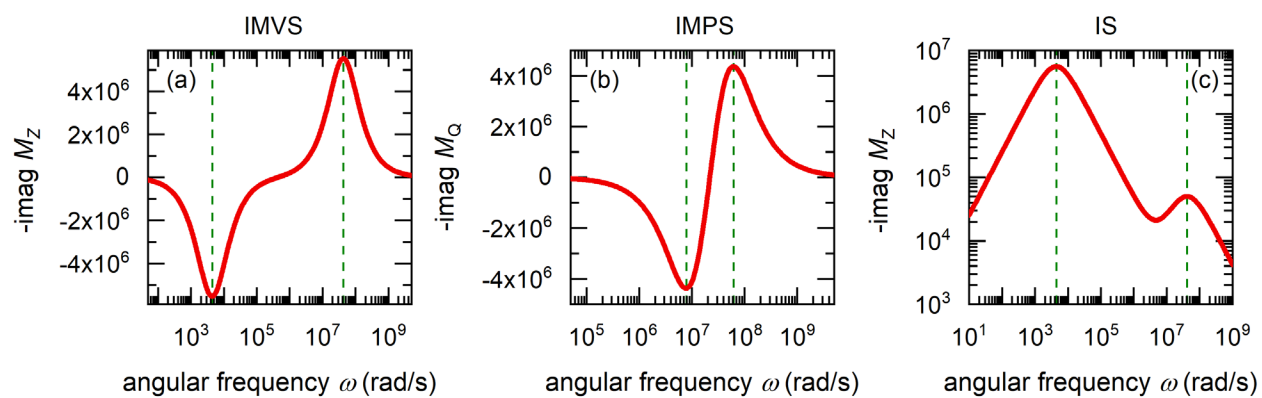
Figure S4 Extrema (dashed lines) of the imaginary part of the transformed (a) IMVS, (b) IMPS and (c) IS transfer functions versus angular frequency, simulated using the equivalent circuit in figure 5 in the main paper. These extrema correspond to the rise and decay time constants.
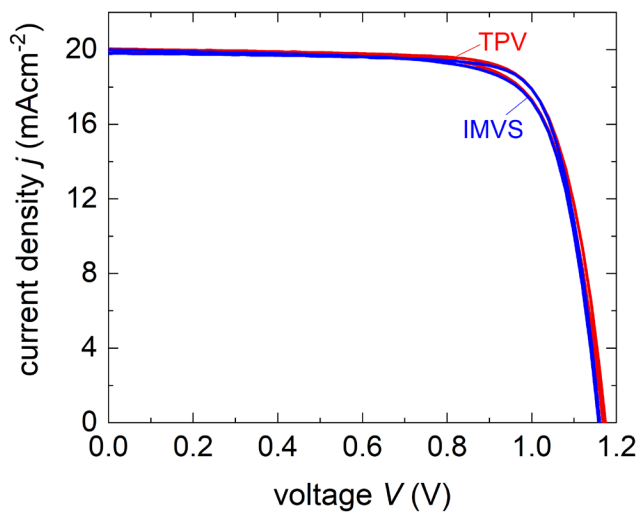

Figure S5 Current-voltage curves of the perovskite solar cells used to make the TPV and IMVS measurements.
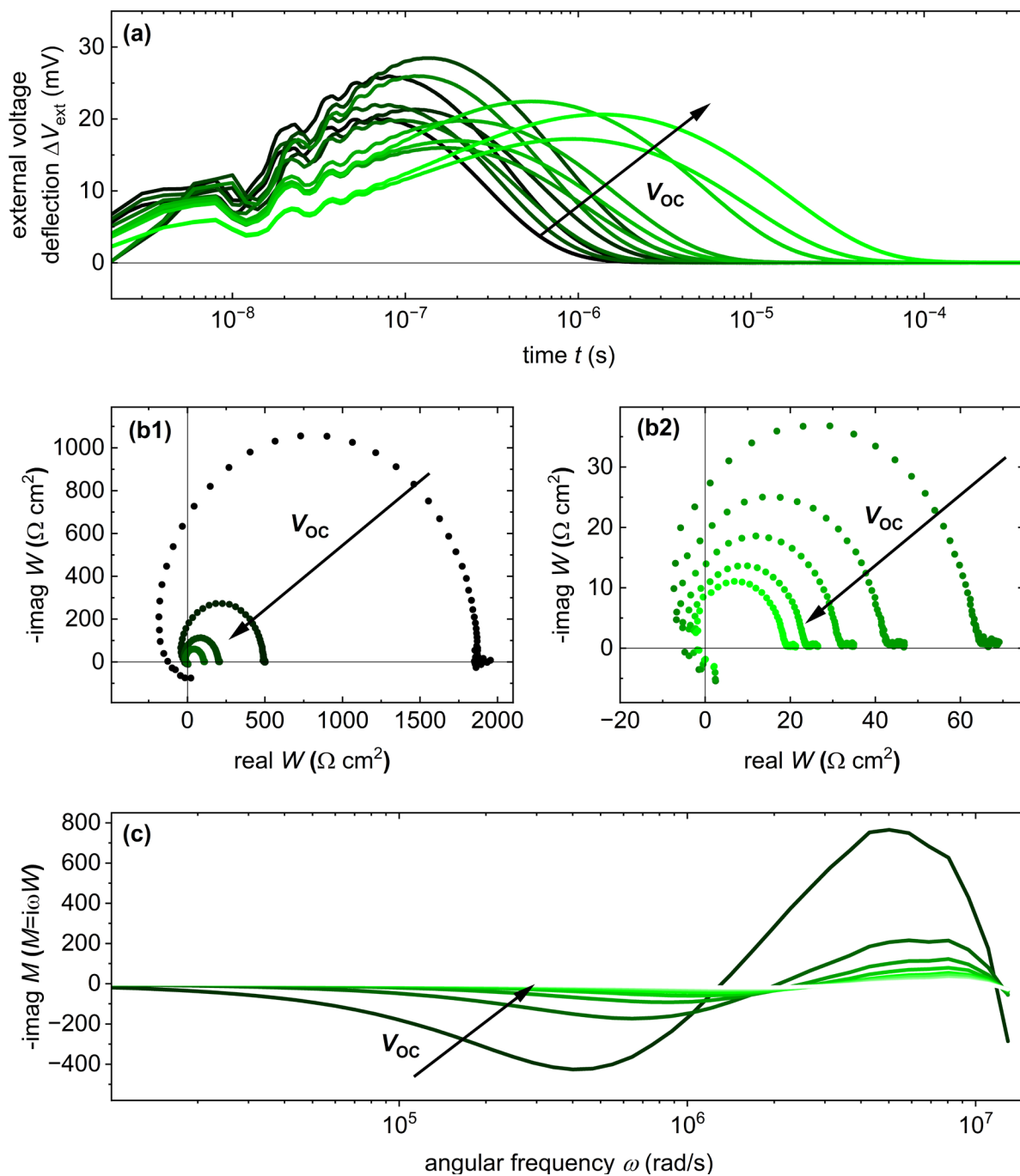
Figure S6 All measured (a) TPV spectra and (b1, b2) real versus negative imaginary parts of the IMVS transfer function W of a $Cs_{0.05}FA_{0.8}MA_{0.15}PbI_{2.25}Br_{0.75}$ perovskite solar cell at different DC open-circuit voltages. (c) shows the negative imaginary part of the transformed IMVS transfer function M_W ($M_W = i\omega W$) versus angular frequency ω, whose peaks correspond to the rise and decay time constants of the photovoltage.
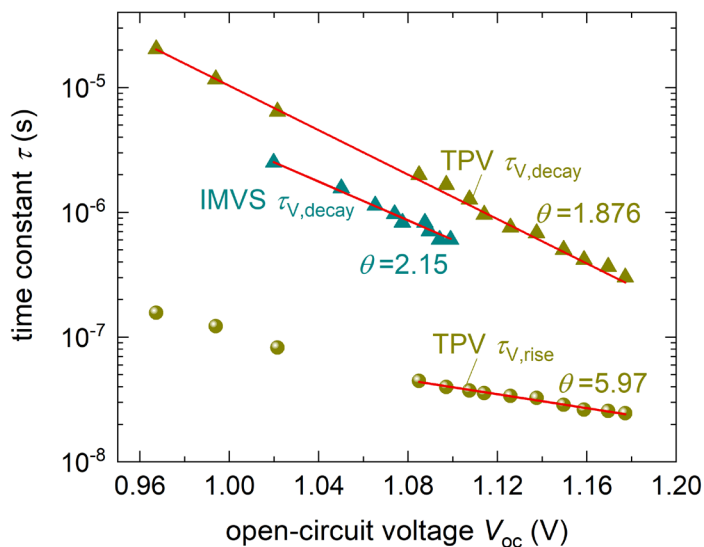
Figure S7 Calculated slope factors θ for the measured IMVS and IS time constants, using equation 25 in the main paper.
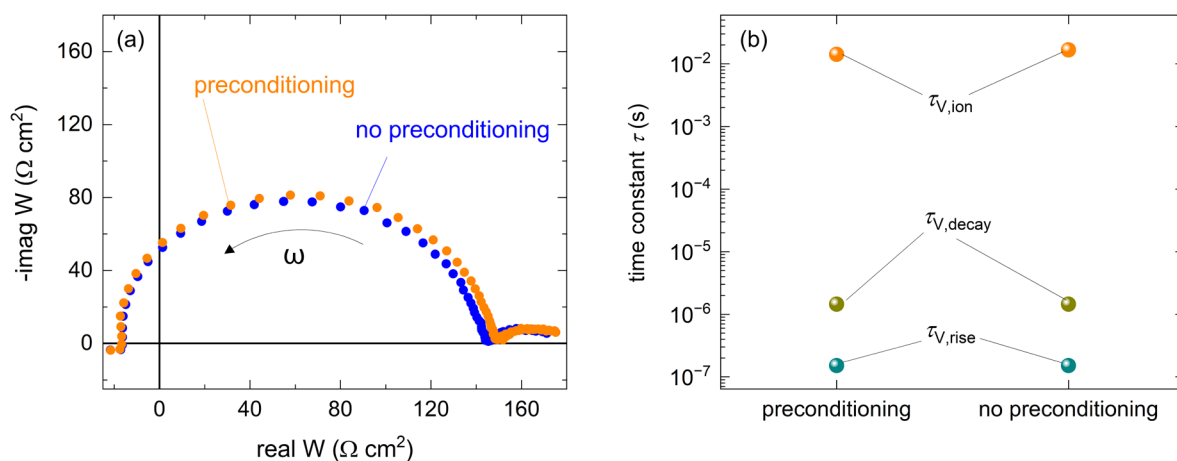

Figure S8 (a) Measured IMVS spectra with and without preconditioning under LED white light illumination (155 W/m^2) at open-circuit condition for 120 seconds. (b) Corresponding rise, decay and low frequency time constants calculated from the data. While the rise and decay time constants remain the same both before and after preconditioning, the magnitude of the low frequency time constant increases upon preconditioning, indicating that it is influenced by the mobile ion density within the perovskite layer.
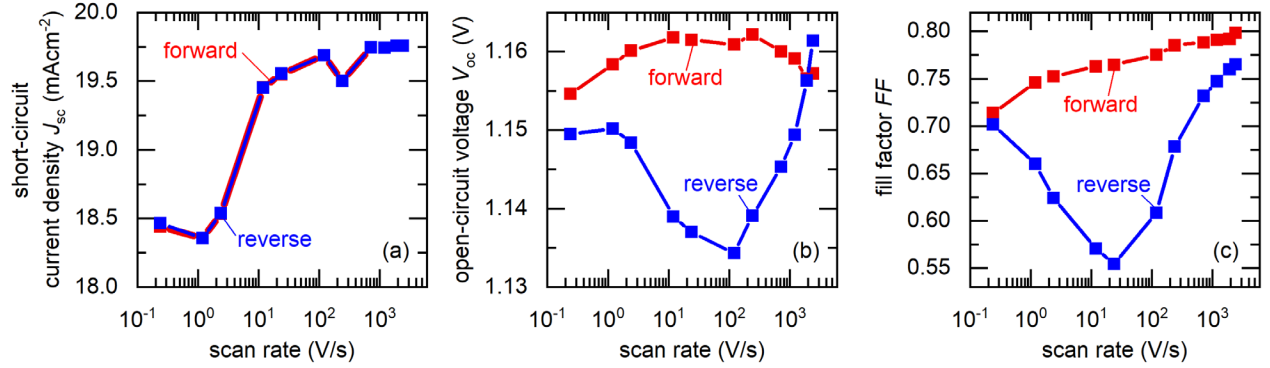
10

Figure S9 Evolution of (a) short-circuit current density, (b) open-circuit voltage and (c) fill factor for current-voltage curves measured at different scan rates, in both the forward and reverse directions. The hysteresis is maximised at intermediate scan rates, while minimised for very fast and very slow scan rates.
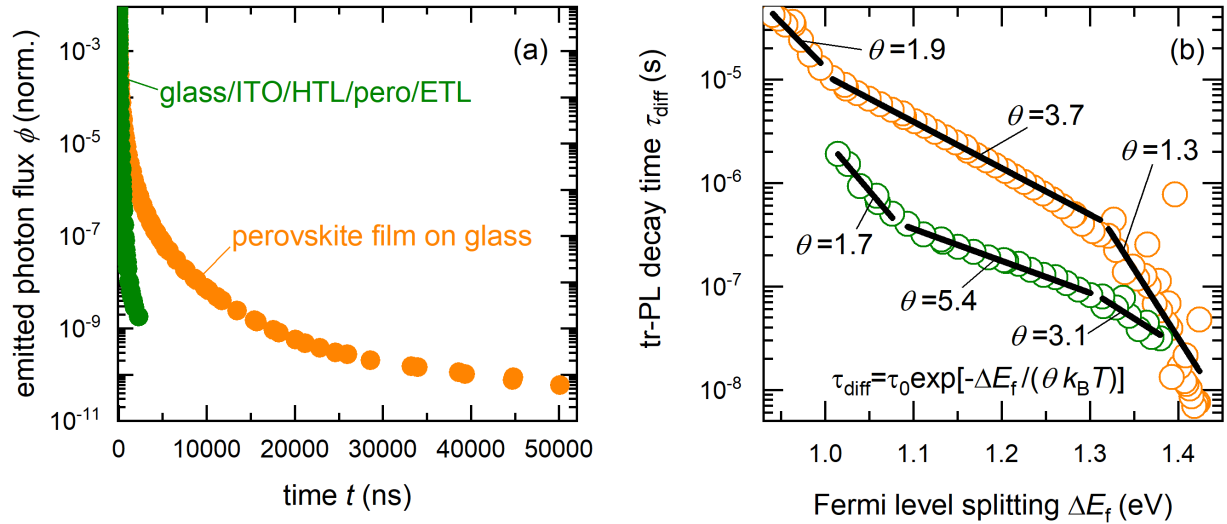
Figure S10 (a) Measured transient photoluminescence spectra of a perovskite film on glass and a glass/ITO/PTAA/ $Cs_{0.05}FA_{0.8}MA_{0.15}PbI_{2.25}Br_{0.75}$/$C_{60}$/BCP stack. (b) shows the calculated decay times (using equation 31 in the main paper) with the fits (using the equation shown in the inset of (b)) and corresponding θ values for three different regions at low, intermediate and high Fermi-level-splitting values.

Table S1 Parameters used to carry out the drift-diffusion simulations using SETFOS, unless stated otherwise in the caption. For TPV simulations, we set an arbitrarily large series resistance ($R_s = 5 \times 10^7$ Ωcm²) to ensure no current flow, while for TPC, we set $R_s = 1$ Ωcm².

parameter	hole transport layer	perovskite	electron transport layer
thickness (nm)	10	300	10
relative permittivity	3	3×10^5	3
electron affinity (eV)	2.33	3.93	3.93
bandgap (eV)	3.2	1.6	2
effective DOS CB (cm⁻³)	10^{18}	10^{18}	10^{18}
effective DOS VB (cm⁻³)	10^{18}	10^{18}	10^{18}
electron mobility (cm²/Vs)	variable	20	variable
hole mobility (cm²/Vs)	variable	20	variable
radiative recombination coefficient (cm³/s)	0	6×10^{-11}	0
acceptor trap energy level (eV)		0.8	
ion density (cm⁻³)		0	
trap density (cm⁻³)		10^{16}	
electron capture coefficient (cm³/s)		10^{-9}	
hole capture coefficient (cm³/s)		10^{-9}	

laser pulse width – 2 nanoseconds.

Table S2 Parameters used to carry out the equivalent circuit simulations in figure 5 in the main paper. No recombination is considered in the transport layers.

parameter	perovskite	transport layers
thickness (nm)	300	10
relative permittivity	30	unneeded
bandgap (eV)	1.6	unneeded
effective DOS CB (cm⁻³)	10^{18}	10^{18}
effective DOS VB (cm⁻³)	10^{18}	10^{18}
electron mobility (cm²/Vs)	unneeded	0.01
hole mobility (cm²/Vs)	unneeded	0.01
radiative recombination coefficient (cm³/s)	6×10^{-11}	
Shockley-Read-Hall recombination lifetime (s)	2×10^{-6}	
built-in electrostatic voltage (V)	unneeded	0.75
ion density (cm⁻³)	0	

series resistance = 1 $\mathbf{\Omega cm^2}$.

Notes and references

1. S. Wheeler, D. Bryant, J. Troughton, T. Kirchartz, T. Watson, J. Nelson and J. R. Durrant, *J. Phys. Chem. C*, 2017, **121**, 13496-13506.
2. R. S. Sanchez, V. Gonzalez-Pedro, J.-W. Lee, N.-G. Park, Y. S. Kang, I. Mora-Sero and J. Bisquert, *J. Phys. Chem. Lett.*, 2014, **5**, 2357-2363.
3. D. Kiermasch, A. Baumann, M. Fischer, V. Dyakonov and K. Tvingstedt, *Energy Environ. Sci.*, 2018, **11**, 629-640.
4. Z. S. Wang, F. Ebadi, B. Carlsen, W. C. Choy and W. Tress, *Small Methods*, 2020, **4**, 2000290.
5. B. C. O'Regan, K. Bakker, J. Kroeze, H. Smit, P. Sommeling and J. R. Durrant, *J. Phys. Chem. B*, 2006, **110**, 17155-17160.
6. L. Krückemeier, Z. Liu, T. Kirchartz and U. Rau, *Adv. Mater.*, 2023, **35**, 2300872.
7. A. Bou, H. Āboliņš, A. Ashoka, H. Cruanyes, A. Guerrero, F. Deschler and J. Bisquert, *ACS Energy Lett.*, 2021, **6**, 2248-2255.
8. J. S. Laird, S. Ravishankar, K. J. Rietwyk, W. Mao, U. Bach and T. A. Smith, *Small Methods*, 2022, **6**, 2200493.
9. W. Peng, C. Aranda, O. M. Bakr, G. Garcia-Belmonte, J. Bisquert and A. Guerrero, *ACS Energy Lett.*, 2018, **3**, 1477-1481.
10. A. J. Riquelme, K. Valadez-Villalobos, P. P. Boix, G. Oskam, I. Mora-Seró and J. A. Anta, *Phys. Chem. Chem. Phys.*, 2022, **24**, 15657-15671.
11. S. Ravishankar, C. Aranda, S. Sanchez, J. Bisquert, M. Saliba and G. Garcia-Belmonte, *J. Phys. Chem. C*, 2019, **123**, 6444-6449.
12. A. O. Alvarez, S. Ravishankar and F. Fabregat-Santiago, *Small Methods*, 2021, **5**, 2100661.
13. A. Guerrero, J. Bisquert and G. Garcia-Belmonte, *Chem. Rev.*, 2021, **121**, 14430-14484.
14. A. Todinova, J. Idígoras, M. Salado, S. Kazim and J. A. Anta, *J. Phys. Chem. Lett.*, 2015, **6**, 3923-3930.
15. A. Pockett, G. E. Eperon, T. Peltola, H. J. Snaith, A. Walker, L. M. Peter and P. J. Cameron, *J. Phys. Chem. C*, 2015, **119**, 3456-3465.
16. B. Hailegnaw, N. S. Sariciftci and M. C. Scharber, *Phys. Status Solidi A*, 2020, **217**, 2000291.
17. A. Riquelme, F. E. Gálvez, L. Contreras-Bernal, H. Míguez and J. A. Anta, *J. Appl. Phys.*, 2020, **128**, 133103.
18. O. Almora, M. García-Batlle and G. Garcia-Belmonte, *J. Phys. Chem. Lett.*, 2019, **10**, 3661-3669.
19. J. Bisquert and M. Janssen, *J. Phys. Chem. Lett.*, 2021, **12**, 7964-7971.
20. E. Ponomarev and L. Peter, *J. Electroanal. Chem.*, 1995, **396**, 219-226.
21. E. Guillén, F. J. Ramos, J. A. Anta and S. Ahmad, *J. Phys. Chem. C*, 2014, **118**, 22913-22922.
22. I. Zarazua, G. Han, P. P. Boix, S. Mhaisalkar, F. Fabregat-Santiago, I. Mora-Seró, J. Bisquert and G. Garcia-Belmonte, *J. Phys. Chem. Lett.*, 2016, **7**, 5105-5113.
23. L. Su, M. Méndez, J. Jiménez-López, M. Zhu, Y. Xiao and E. J. P. Gil, *ChemPlusChem*, 2021, **86**, 1316-1321.
24. C. R. McNeill, I. Hwang and N. C. Greenham, *J. Appl. Phys.*, 2009, **106**, 024507.
25. M. Neukom, S. Züfle, S. Jenatsch and B. Ruhstaller, *Sci. Technol. Adv. Mater.*, 2018, **19**, 291-316.
26. S. Ravishankar, Z. Liu, Y. Wang, T. Kirchartz and U. Rau, *PRX Energy*, 2023, **2**, 033006.
27. M. Cai, N. Ishida, X. Li, X. Yang, T. Noda, Y. Wu, F. Xie, H. Naito, D. Fujita and L. Han, *Joule*, 2018, **2**, 296-306.
28. C. Stavrakas, G. Delport, A. A. Zhumekenov, M. Anaya, R. Chahbazian, O. M. Bakr, E. S. Barnard and S. D. Stranks, *ACS Energy Lett.*, 2020, **5**, 117-123.
29. L. M. Herz, *ACS Energy Lett.*, 2017, **2**, 1539-1548.
30. W. Shockley and W. Read Jr, *Phys. Rev.*, 1952, **87**, 835.
31. M. H. Futscher, J. M. Lee, L. McGovern, L. A. Muscarella, T. Wang, M. I. Haider, A. Fakharuddin, L. Schmidt-Mende and B. Ehrler, *Mater. Horiz.*, 2019, **6**, 1497-1503.
32. R. A. Awni, Z. Song, C. Chen, C. Li, C. Wang, M. A. Razooqi, L. Chen, X. Wang, R. J. Ellingson and J. V. Li, *Joule*, 2020, **4**, 644-657.
33. M. Azzouzi, P. Calado, A. M. Telford, F. Eisner, X. Hou, T. Kirchartz, P. R. F. Barnes and J. Nelson, *Solar RRL*, 2020, **4**, 1900581.
34. D. Cardenas-Morcoso, A. Bou, S. Ravishankar, M. García-Tecedor, S. Gimenez and J. Bisquert, *ACS Energy Lett.*, 2020, **5**, 187-191.
35. A. Pockett, M. Spence, S. K. Thomas, D. Raptis, T. Watson and M. J. Carnie, *Solar RRL*, 2021, **5**, 2100159.
36. L. J. Bennett, A. J. Riquelme, J. A. Anta, N. E. Courtier and G. Richardson, *Phys. Rev. Appl.*, 2023, **19**, 014061.
37. V. M. Le Corre, J. Diekmann, F. Peña-Camargo, J. Thiesbrummel, N. Tokmoldin, E. Gutierrez-Partida, K. P. Peters, L. Perdigón-Toro, M. H. Futscher, F. Lang, J. Warby, H. J. Snaith, D. Neher and M. Stolterfoht, *Solar RRL*, 2022, **6**, 2100772.
38. J. Thiesbrummel, V. M. Le Corre, F. Peña-Camargo, L. Perdigón-Toro, F. Lang, F. Yang, M. Grischek, E. Gutierrez-Partida, J. Warby, M. D. Farrar, S. Mahesh, P. Caprioglio, S. Albrecht, D. Neher, H. J. Snaith and M. Stolterfoht, *Adv. Energy Mater.*, 2021, **11**, 2101447.

39.   H. Wang, A. Guerrero, A. Bou, A. M. Al-Mayouf and J. Bisquert, *Energy Environ. Sci.*, 2019, **12**, 2054-2079.
40.   L. Krückemeier, B. Krogmeier, Z. Liu, U. Rau and T. Kirchartz, *Adv. Energy Mater.*, 2021, **11**, 2003489.
41.   L. Krückemeier, Z. Liu, B. Krogmeier, U. Rau and T. Kirchartz, *Adv. Energy Mater.*, 2021, **11**, 2102290.
42.   D. Grabowski, Z. Liu, G. Schöpe, U. Rau and T. Kirchartz, *Solar RRL*, 2022, **6**, 2200507.
43.   U. Rau, V. Huhn and B. E. Pieters, *Phys. Rev. Appl.*, 2020, **14**, 014046.
44.   R. S. Crandall, *J. Appl. Phys.*, 1983, **54**, 7176-7186.
45.   Y. Yuan, G. Yan, C. Dreessen, M. Hülsbeck, B. Klingebiel, U. Rau and T. Kirchartz, *Res. Sq. preprint*, 2023, URL: https://assets.researchsquare.com/files/rs-2514593/v1/0398c512303ecfd5def49f7d.pdf?c=1674796116.
46.   Y. Wang, S. Akel, B. Klingebiel and T. Kirchartz, *Adv. Energy Mater.*, 2023, 2302614.
47.   M. Stolterfoht, P. Caprioglio, C. M. Wolff, J. A. Márquez, J. Nordmann, S. Zhang, D. Rothhardt, U. Hörmann, Y. Amir and A. Redinger, *Energy Environ. Sci.*, 2019, **12**, 2778-2788.
48.   S. Sami, P. A. Haase, R. Alessandri, R. Broer and R. W. Havenith, *J. Phys. Chem. A*, 2018, **122**, 3919-3926.
49.   M. Sendner, P. K. Nayak, D. A. Egger, S. Beck, C. Müller, B. Epding, W. Kowalsky, L. Kronik, H. J. Snaith and A. Pucci, *Mater. Horiz.*, 2016, **3**, 613-620.
50.   Z. Liu, L. Krückemeier, B. Krogmeier, B. Klingebiel, J. A. Márquez, S. Levcenko, S. Öz, S. Mathur, U. Rau, T. Unold and T. Kirchartz, *ACS Energy Lett.*, 2019, **4**, 110-117.
51.   J. Maibach, E. Mankel, T. Mayer and W. Jaegermann, *J. Mater. Chem. C*, 2013, **1**, 7635-7642.
52.   F. Staub, H. Hempel, J.-C. Hebig, J. Mock, U. W. Paetzold, U. Rau, T. Unold and T. Kirchartz, *Phys. Rev. Appl.*, 2016, **6**, 044017.